Ionospheric midlatitude electric current density inferred from multiple magnetic satellites

R. M. Shore,[1] K. A. Whaler,[1] S. Macmillan,[2] C. Beggan,[2] N. Olsen,[3] T. Spain,[4] and A. Aruliah[4]

[1]   A method for inferring zonal electric current density in the mid-to-low latitude F region ionosphere is presented. We describe a method of using near-simultaneous overflights of the Ørsted and CHAMP satellites to define a closed circuit for an application of Ampère's integral law to magnetic data. Zonal current density from sources in only the region between the two satellites is estimated for the first time. Six years of mutually available vector magnetic data allows overlaps spanning the full 24 h range of local time twice. Solutions are computed on an event-by-event basis after correcting for estimates of main and crustal magnetic fields. Current density in the range $\pm 0.1\ \mu\text{A/m}^2$ is resolved, with the distribution of electric current largely matching known features such as the Appleton anomaly. The currents appear unmodulated at times of either high-negative Dst or high $F_{10.7}$, which has implications for any future efforts to model their effects. We resolve persistent current intensifications between geomagnetic latitudes of 30 and 50° in the postmidnight, predawn sector, a region typically thought to be relatively free of electric currents. The cause of these unexpected intensifications remains an open issue. We compare our results with current density predictions made by the Coupled Thermosphere-Ionosphere-Plasmasphere model, a self-consistent, first-principles, three-dimensional numerical dynamic model of ionospheric composition and temperatures. This independent validation of our current density estimates highlights good agreement in the broad spatiotemporal trends we identify, which increases confidence in our results.

Citation: Shore, R. M., K. A. Whaler, S. Macmillan, C. Beggan, N. Olsen, T. Spain, and A. Aruliah (2013), Ionospheric midlatitude electric current density inferred from multiple magnetic satellites, *J. Geophys. Res. Space Physics*, *118*, 5813–5829, doi:10.1002/jgra.50491.

1.   Introduction

[2]   Magnetic field research has greatly benefitted over the past decade from an abundance of high-accuracy satellite-sampled data obtained at low-Earth orbit (LEO). The spacecraft fly through the magnetized plasma of the ionosphere in which a complex array of electric currents flow in both the day and night sectors. The currents contribute to the measured magnetic field, violating the assumption of measurement in a source-free region—a requirement of magnetic field representations which adopt a scalar potential. Data selection techniques are commonly employed to lessen the effect of these unwanted contributions, which requires a good understanding of the distribution and magnitude of the currents. Much work has been published on their description and quantification with single satellite measurements, for example, by *Olsen* [1997], *Lühr et al.* [2002], *Maus and Lühr* [2006], and *Lühr and Maus* [2006]. However, when using a single satellite to estimate electric current density, it is difficult to avoid biasing the estimates by inclusion of contributions from regions outside the satellites' altitude range. This can be ameliorated in part by making geometrical assumptions about the regions being studied (or avoided), as in, for example, *Juusola et al.* [2007]. Here we detail for the first time, multi-satellite estimated trends in the zonal ionospheric electric current density at a range of local time (LT) and phases of the solar cycle. The orbits of the Ørsted and CHAMP satellites are near-polar-crossing with altitudes of 650–860 km and 460–350 km, respectively [*Neubert et al.*, 2001; *Reigber et al.*, 2002]. We apply Ampère's law integral to overflights of the satellites to resolve total current flow in solely the region between the two orbits at mid-to-low latitudes on an event-by-event basis, though we acknowledge this approach precludes a global perspective. We analyze, in detail, the observed trends in current density and describe their causes.

[1]School of GeoSciences, Grant Institute, University of Edinburgh, Edinburgh, UK.
[2]British Geological Survey, Edinburgh, UK.
[3]DTU Space, National Space Institute, Technical University of Denmark, Kongens Lyngby Denmark.
[4]Atmospheric Physics Laboratory, Department of Physics and Astronomy, University College London, London, UK.

Corresponding author: R. M. Shore, British Antarctic Survey, High Cross, Madingley Road, Cambridge CB3 OET, UK. (robore@bas.ac.uk)

[3] In section 2, we discuss the relevant electrodynamic processes in the mid-to-low latitude ionosphere. In section 3, we outline the method used to calculate ionospheric current density from satellite magnetic data. In section 4, we provide an overview of the current density estimates and compare them with predictions made by an upper atmospheric physics model. We summarize the conclusions in section 5. Appendices A and B describe the methods of rotation to the along-track frame and calculation of the integral area in detail, respectively. Appendix C shows the criteria used to prevent geometric errors from biasing the estimates, and in Appendix D, we assess the impact of likely sources of error in the current density estimates.

2. Low-Latitude Ionospheric Electrodynamics

[4] Within the mesosphere and thermosphere, the E and F regions of the ionosphere span altitudes of 90–140 km and 140–1000 km, respectively [*Kelley*, 2009]. Utilizing the overflight configuration of the Ørsted and CHAMP satellites allows resolution of predominantly zonal electric currents flowing between them at mid-to-low latitudes. The geometry of the overflights precludes analysis of the currents at high latitudes, as we discuss further in the appendices. At F region altitudes, the major zonal electric current sources are due to the action of Lorentz, gravity, and pressure gradient forces, with the full distribution of current density given by [*Lühr et al.*, 2008; *Alken et al.*, 2011]

$$\mathbf{J} = \underline{\underline{\sigma}} \, (\mathbf{E} + \mathbf{U} \times \mathbf{B})$$
$$+ \{N_e m_i \mathbf{g} \times \mathbf{B} - k\nabla\left[(T_i + T_e) N_e\right] \times \mathbf{B}\} \, \frac{1}{B^2}, \qquad (1)$$

where $\mathbf{J}$ is the current density, $\underline{\underline{\sigma}}$ the conductivity tensor [*Forbes*, 1981], $\mathbf{E}$ the electric field, $\mathbf{U}$ the neutral wind velocity, N_e the electron density, m_i the ion mass, $\mathbf{g}$ the gravitational acceleration, k Boltzmann's constant, T_i and T_e the ion and electron temperatures, and $\mathbf{B}$ the ambient magnetic field with magnitude B.

[5] This study uses the geographic (GEO) system of spherical polar coordinates $(r, \theta, \text{and } \phi)$, where r is the length of the radial position vector from Earth's center (and "altitude" is the part of r above the reference sphere of radius 6371.2 km), θ (colatitude) is the angle between the Earth's rotation axis and the radial vector, and ϕ (longitude) is the angle in the equatorial plane between the Greenwich meridian and the radial vector [e.g., *Hapgood*, 1992].

[6] The first term in equation (1) is the combination of the electric and magnetic Lorentz forces, modulated by Ohm's law via the conductivity tensor [*Rishbeth*, 1988; *Kivelson and Russell*, 1995], and describes the major ionospheric dynamo system currents such as Sq (Solar-quiet) and the equatorial electrojet (EEJ) [*Alken et al.*, 2011]. These current systems result from the tendency for the ionosphere to build up electric charges at boundaries of conductivity, thus creating secondary "polarization" electric fields which in turn cause secondary currents [*Amm et al.*, 2011]. *Cowling* [1932] was the first to recognize this property of the ionosphere. The direction of $\mathbf{B}$ is the primary controlling factor for the anisotropy of ionospheric conductivity and the resulting direction of the electric currents, since the motion of charged particles across magnetic field lines is impeded to a far greater degree than motion along the field lines. The

strength of the electric current is modulated by the concentration of plasma, which electric, gravity, and pressure forces push across magnetic field lines. The two parts of the second term in equation (1) describe the gravity and pressure gradient electric currents, respectively. *Rishbeth* [1988] described the electric forcing, while *Goldberg* [1965] discussed the gravity and pressure driven currents (neglecting the effect of neutral air winds). While the ionosphere as a whole can reasonably be defined as horizontally stratified, the electrodynamic coupling of the E and F regions produces complex structure and marked meridional gradients in the plasma distribution, thus affecting the distribution of electric currents. In our area of interest, the largest of these structures is the Appleton anomaly [*Appleton*, 1946], also known as the equatorial ionization anomaly (EIA), characterized by two "crests" of enhanced plasma density flanking the magnetic dip equator at tropical latitudes [*Alken and Maus*, 2010; *Alken et al.*, 2011]. The EIA is the main ionospheric phenomenon resolved in this study—here we will briefly describe the electrodynamic environment affecting it.

[7] In the equatorial dayside F region, a vertical upward drift of plasma (both ions and electrons) across the magnetic field lines is driven by $E_\phi \times B_\theta$ action, a process generalized by *Kivelson and Russell* [1995]. Here E_ϕ refers to the zonal component of the electric field ($\mathbf{E}$ in equation (1)) resulting from dynamo action at low latitudes and midlatitudes in both the E and F regions. The vertical drift lifts the plasma to altitudes of around 800 km at the equator [*Balan and Bailey*, 1995b; *Bailey et al.*, 1997]. Under the action of pressure and gravity, the plasma diffuses downward and poleward along the magnetic field lines to form the EIA crests at about $\pm 15°$ dip latitude and 400 km altitude [*Mitra*, 1946; *Huang*, 1974]. Despite higher loss rates at lower altitudes, the action of this "plasma fountain" [*Balan and Bailey*, 1995a] is sufficient to develop the EIA, and the F region then has a higher plasma density at altitudes of 400 km than it does around 200 km [*Rishbeth*, 1988]. The plasma crests rise in the F region throughout daytime, descending and becoming more bifurcated after sunset, and disappear almost completely before dawn. The interaction of the E and F region dynamos at the dusk terminator is called the prereversal enhancement (PRE). This mechanism, described by *Kelley* [2009] and *Heelis* [2004], is in essence a dusk-centered enhancement of the zonal electric field. This enhancement causes an acceleration in the rates of $\mathbf{E} \times \mathbf{B}$ plasma uplift, affecting the LT distribution of the EIA and reducing the plasma density at lower F region altitudes.

[8] The distribution of zonal current density at the altitudes of the Ørsted and CHAMP satellites in LT can be understood by the distribution of the zonal electric field strength, the dynamo action of the neutral winds, and the plasma density accumulations related to the EIA. The tendency for stronger zonal current near the dip equator is due to the latitude distribution of the EIA, increasing the Pedersen conductivity through collisional processes, as well as providing more plasma for gravity and pressure gradient forces to act upon. There are other less important sources of zonal current in the low-latitude F region, such as the electric polarization fields produced by the divergence of the gravity and pressure gradient currents, and the effect of impinging electric fields from high latitude and
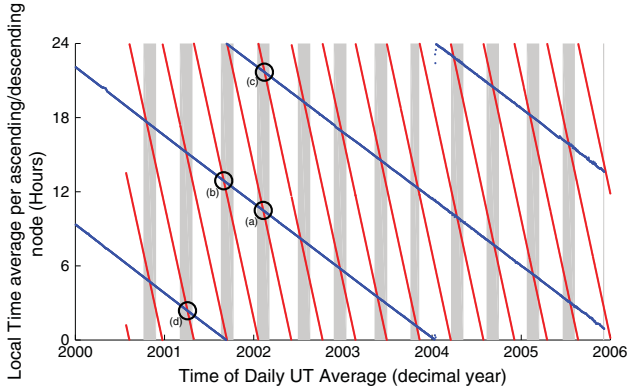
Figure 1. Available local time overlaps. Daily local time averages at midlatitude for the ascending and descending nodes of the Ørsted (blue) and CHAMP (red) satellites. Shaded regions indicate ± 2 h local time proximity of CHAMP to Ørsted. These data are interpolated: missing data affect the true overlap distribution. The black circles labeled (a) to (d) indicate the overlaps shown in the four panels of Figure 3.

magnetospheric processes. The relative importance of these effects at low latitudes is an open issue in ionospheric physics [*Kelley*, 2009].

3. Method Overview

[9] Several efforts have been made to resolve electric current density estimates using magnetic data from satellites. Besides the recent studies mentioned in section 1, we also note the study of *Suzuki et al.* [1982], who were the first to apply Ampère's integral to satellite magnetic data. To develop our method of resolving event-by-event in situ current density estimates from satellite data, we draw on two recent approaches in particular. *Stauning and Primdahl* [2000] integrated signal from half-orbits of Ørsted to resolve cross-polar-cap current flow. They demonstrated a relatively small error arising from fictitiously closing the integral loop via the equator. *Ritter and Lühr* [2006] described a method that could be used to resolve radial current density (projected onto the field-aligned direction) from the side-by-side configuration of the two lower-altitude satellites in the upcoming *Swarm* multisatellite constellation mission of the European Space Agency (ESA). The basic process we use is an application of Ampère's law, which relates the satellite magnetic field measurements **B** to the current I flowing through a closed loop:

$$\oint \mathbf{B} \cdot \mathbf{dl} = \mu_0 I, \qquad (2)$$

where **dl** is a series of line elements which comprise the closed circuit and μ_0 is the permeability of free space $(4\pi \cdot 10^{-7}$ T m/A). In this case, the closed circuit is a near-simultaneous overflight of Ørsted and CHAMP.

[10] CHAMP and Ørsted have shared vector data coverage in the years 2000 to 2006. Within this period, we compare the mean LT of each daily magnetic vector data file for both Ørsted and CHAMP. Those which are within ± 2 h

of one another are retained (termed an epoch). The full set of epochs is shown in Figure 1—each contains two LT sectors of orbital overlaps. These overlaps span the set of LTs twice, though the data coverage within these epochs is affected by data missing from Ørsted's ideal coverage. The impact of even short time spans of missing data is further exacerbated by the narrow UT (universal time) band in which the valid overlaps lie.

[11] Within each epoch, the most closely spatially overlapping tracks of satellite data are selected in the geographic coordinate frame. At each overlap point, we define contributing tracks of satellite data from Ørsted and CHAMP, each chosen to be an arc of length 2° in geographic colatitude (assuming no missing data), equal to the minimum radial spacing between the two orbits. Shorter arc-lengths do not increase the spatial or temporal resolution of the currents and are proportionally more affected by missing data. Ørsted and CHAMP have sampling intervals of 1.135 and 1 s, respectively, and each take around 30 s to cover the length of the arc. The integral loop is constructed from the two arcs, leading to around 70 data points in each loop.

[12] The ECEF (Earth-centered, Earth-fixed) Cartesian coordinate system (hereafter "Cartesian coordinates") is defined such that the x axis points from the center of the Earth toward the Greenwich meridian in the geographic equatorial plane. The z axis points toward geographic North, and the y axis completes the right-hand triad [e.g., *Hapgood*, 1992; *Langel and Hinze*, 1998]. The **dl** in equation (2) are formed in the integral loop from each successive pair of data points in the Cartesian frame as follows

$$\mathbf{dl} = (x_2 - x_1, \; y_2 - y_1, \; z_2 - z_1). \qquad (3)$$

Each line element defines the "along-track" direction at that point in the integral loop. Since the relative flight directions of Ørsted and CHAMP reverse each epoch, we force the integral direction in each case to be north-to-south for Ørsted, and south-to-north for CHAMP, resulting in a consistent direction for the calculations, by which the convention for the subscripts 1 and 2 is defined. On the upper and lower parts of the loop, we form the line elements from the successive measurement points of the satellites. The radial connecting elements of the circuit have no data coverage between their endpoints, but still represent a part of the loop bridging two measurement points as we treat the radial elements in an identical manner to the line elements formed in the satellite tracks.

[13] We do not apply data selection criteria prior to the calculation of the integral solution. From the magnetic data (**B**) in each pair of arcs, we remove core (**B**$_{core}$) and crustal (**B**$_{crust}$) field estimates using the CHAOS-2 [*Olsen et al.*, 2009] and comprehensive model (CM4) [*Sabaka et al.*, 2004] models, respectively, producing the perturbation vector data $\Delta\mathbf{B}$ from

$$\Delta\mathbf{B} = \mathbf{B} - \mathbf{B}_{core} - \mathbf{B}_{crust}. \qquad (4)$$

The effect of the crustal signal is not a significant factor in the results, due to its low amplitude at F region altitudes. We rotate both $\Delta\mathbf{B}$ and **dl** using the process detailed in Appendix A, resulting in $\Delta\mathbf{B}_{AT}$ and $\mathbf{dl}_{AT}$ in the along-track frame. The along-track component for each of the magnetic perturbation vectors is now their respective x components.
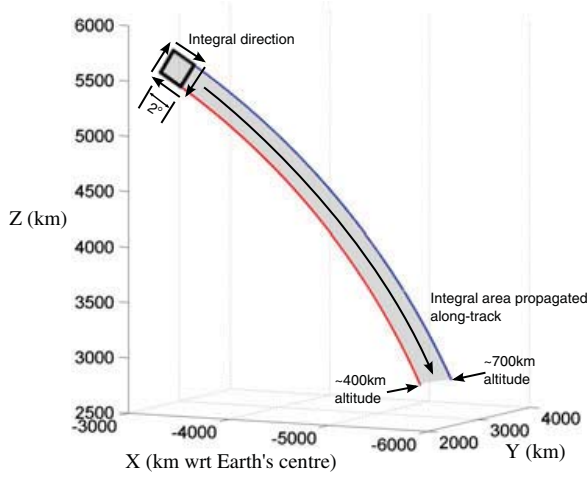
Figure 2. Cartesian coordinate geometry of overflight region and integral solution area setup. The Cartesian coordinate system is defined in Appendix A. Ørsted data locations shown as a part-orbit of blue dots, CHAMP as red. The black square indicates a circuit defined from an overflight of length 2° colatitude for each satellite. Note the lack of data on the radial connecting elements of the circuit. The arrows show the direction of integration, resulting in eastward current flow being positive. The length of the longer arcs is the same as the distance the 2° setup will be migrated along-orbit, producing a solution at each Ørsted data point spacing. The shaded region indicates the area over which current is integrated.

The mean magnetic perturbation vector in the integration direction for a single line element is then

$$\Delta \mathbf{B}_{AT} = (\Delta \mathbf{B}_{2AT} + \Delta \mathbf{B}_{1AT})/2. \qquad (5)$$

[14] The contribution of each line element to the integral current of equation (2) is the dot product of $\Delta \mathbf{B}_{AT}$ and $\mathbf{dl}_{AT}$. We obtain the current density J flowing normal to the integral loop by dividing the summed current value by the area A (calculated via triangulation as described in Appendix B) enclosed by the two satellite tracks, as follows

$$J = \frac{\sum_{i=1}^{n} \Delta \mathbf{B}_{ATi} \cdot \mathbf{dl}_{ATi}}{\mu_0 A}, \qquad (6)$$

where n is the number of line elements in the integral circuit, equal to the number of data points.

[15] Figure 2 shows a 24°-long arc span of Ørsted and CHAMP data, with a typical integral calculation region (and its integration direction) superimposed. We find that these arc setups can be stably propagated along-orbit up to 12° colatitude in each direction from the crossover's center-point, to increase data density. The along-orbit propagation involves incrementing the 2°-long Ørsted arc by one data point, and finding the best-fitting CHAMP arc underneath it, providing many integral loops within the 24°-long arc span.

[16] At this stage in the process, we have applied very broad temporal and spatial criteria for selecting overflights, so the data set contains overflights which overlap in time

but not closely in space, and vice versa. We winnow the set of along-orbit propagated overlaps to a smaller set of viable solutions using the (principally geometry-based) rejection criteria summarized in Appendix C. These rejection criteria are defined following the results (not shown) of real and synthetic data tests, establishing the effect of the factors listed in Appendix C on the current density estimates. After applying the rejection criteria, we are left with our final data set of overlaps for the epoch being processed. It is important to note that while the rejection criteria are as stringent as possible, we cannot correct for the possibility of errors inherent to the method itself, most notably from the altitude difference between the two satellites. These errors, including the error introduced by the along-orbit propagation, are offset by careful selection and treatment of overlaps as discussed in Appendix D, and they are shown to have no detrimental effect on the results we present in the next section. The full integration procedure described above (and in the appendices) is applied to every viable overlap within the 6 year time span of mutually available vector data from Ørsted and CHAMP.

[17] The method discussed above can be used to obtain estimates of the average zonal electric current density in a three-dimensional loop defined between two satellites at different altitudes. The method requires certain simplifying assumptions—for instance, although it is unlikely that the current is homogeneous between the two satellite altitudes, our method can only estimate the average current density and so is blind to departures from linear vertical trends in the currents. The bias introduced by this altitude difference is quantified in section 4.3, and leads to a consistent underestimate of current density trends (in which between 20% and 40% of the signal is lost) by the method we have applied. However, the magnitude of the variance in the trends discussed in the next section is greater than this consistent loss of signal.

[18] Further to the errors inherent to the integration method, the lack of any averaging in our representation of isolated LT sectors means that at any point, the current density estimates could be subject to effects from the following controlling factors: solar activity, geomagnetic activity, season, longitude sector, colatitude, and LT. These effects cannot be accounted for in the rejection criteria summarized in Appendix C. The combination of our limited data coverage and the controlling factors precludes us from obtaining a coherent global picture of the currents. However, these drawbacks are acceptable given the purpose of the method—to resolve only the currents affecting satellite magnetic data at the measurement altitude. A multi-satellite approach is preferable to the use of a single satellite in meeting these aims, since it obviates the need to parametrize (with inevitable error) the much stronger current contributions from above and below the satellites' altitudes, and allows event-by-event resolution of current density, removing the need to rely on a statistical approach. Since we estimate current density on an event-by-event basis, we are able to use any high-frequency (in colatitude) error highlighted by the along-orbit propagation as a check for the self-consistency of the current density solutions. We assess the effect of each of the controlling factors in section 4.1—our method is surprisingly resilient to these errors. In section 4.2, we use an ionospheric model to compare our estimates with
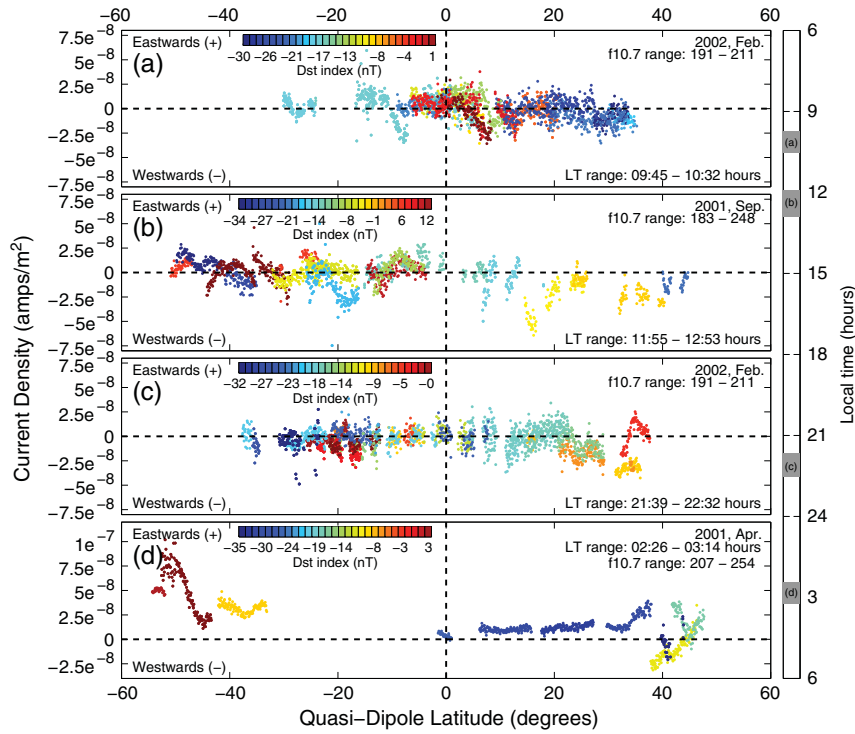
Figure 3. Solutions for zonal electric current density from the Ørsted/CHAMP overflights in four LT bands progressing from day through night: (a) 09:45 to 10:32 h, (b) 11:55 to 12:53 h, (c) 21:39 to 22:32 h, and (d) 02:26 to 03:14 h. Each subplot contains results from about 15 days in UT (noncontinuous recording), in a band of LT roughly 1 h wide. Each data point is the integral-area-normalized result of applying Ampère's integral to a single overflight of length 2° colatitude. The points are colored by samples of the *Dst* (disturbance storm time) index. Eastward current flow is positive; westward negative. The units of $F_{10.7}$ in the overlays are 10^{-22} W/m²/Hz.

a set of global "typical" ionospheric background current density estimates.

4. Results

4.1. Local Time Sector Analysis

[19] Some systematic, global-scale features of the current density estimates are as follows. On the dayside, the estimated current flow is stronger in the westward direction and has higher magnitude than on the nightside. In terms of latitude, the dayside current density is stronger near the dip equator than toward the poles (appearing to follow the EIA distribution). On the nightside, the current has no strong direction preference and exhibits weak latitudinal trends until after midnight, when the current density is strongest in the midlatitudes. The magnitude of the current density estimates all lie within the range ± 0.1 μA/m² (once solutions deemed to be invalid are rejected as per the criteria in Appendix C). This is within the range reported by *Ritter and Lühr* [2006], though they focused on field-aligned currents at higher latitudes. *Olsen* [1997] used data from Magsat (altitude range between 350 and 550 km) to resolve meridional horizontal mean current density at dusk. Values in the range −30 to +60 nA/m² were obtained for the J_θ component between magnetic latitudes of ±30°. At dusk, our Ørsted/CHAMP results for low-latitude zonal current

density (J_ϕ) are in remarkably good agreement with the magnitude range of Olsen's Magsat values for J_θ, though typically occupy the lower magnitudes within this range. This difference is to be expected as the J_θ component will have a larger contribution from the interhemispheric field-aligned currents (FACs) which permeate the *F* region. Even if we were to measure J_θ, a difference in the results from Ørsted/CHAMP and Magsat would be expected due to the fact that the Magsat results are mean values (temporally smoothed), while the Ørsted/CHAMP results are instantaneous estimates. These have never been estimated at LEO altitude from multi-satellite magnetic data before, and we do not expect a perfect match with previous estimates. Yet from the comparisons presented here, the Ørsted/CHAMP results appear reasonable.

[20] We do not have current density estimates at all LTs as a continuous data set, since the data are recorded at times months apart, in different geomagnetic conditions, and at different points in the solar cycle. However, the specific trends shown and discussed in this section all occur in more than one epoch and exhibit similar forms at different geomagnetic, seasonal, and solar conditions. Thus, we consider the trends discussed here robust, and representative of the electrodynamics of the upper *F* region ionosphere at the set of local times shown.

[21] Figures 3a–3d show electric current density estimates from four sectors of LT, each from a different series of

overlaps as indicated in Figure 1. The sector in Figure 3d has a different range to the other subplots, but the figure uses a consistent vertical scale (all sectors span $0.16 \ \mu A/m^2$). We have selected these particular epochs because they are among the "quietest," geomagnetically speaking, and are the least affected by biases to the integral method (discussed in more detail in Appendix D). Each subplot of Figure 3 contains results spanning roughly 15 days in UT (noncontinuous recording), in a band of LT approximately 1 h wide. The approximate UT range (hence, season) and precise LT range are shown as text in the right-hand part of each subplot. The accompanying range of $F_{10.7}$ solar flux density denotes the extrema of this index (daily values) throughout the UT span of the particular overlap series. Note that gaps in the colatitude coverage indicate missing data from one or more satellites, and do not imply zero values for the resolved current. We have used Quasi-Dipole (QD) latitude [*Richmond*, 1995] to keep the magnetic dip equator at $0°$. Each data point is the result of applying Ampère's integral to a single Ørsted/CHAMP overflight of length $2°$ colatitude— eastward current flow is positive, and westward negative. The points are colored according to the *Dst* (disturbance storm time) index, a measure of global mid-to-low latitude geomagnetic field activity. We include these sampled data to show their lack of effect on the trends we discuss. The sampled *Dst* does not exceed "medium" activity levels, and we have checked the sampling times of the epochs to ensure that they are not in geomagnetic storm recovery periods (which can have low *Dst*, but an energetic ionosphere). Analysis (not shown) of the entire set of current density estimates shows no clear correlation with *Dst* at either high negative (up to -140 nT) or low values of this index. We note that similar attempts (not shown) to identify relationships between the current density estimates and solar activity (via $F_{10.7}$ solar flux density), or longitude sector, also exhibit a lack of correlation. The lack of dependence on $F_{10.7}$ persists despite the occasionally high values sampled in the epochs discussed in this section. Globally speaking, the current density estimates are most strongly organized in LT and colatitude (hence, they are assessed in this frame here). This indicates that the estimates respond most strongly to the plasma density accumulations of the EIA. The direction (sign) of the currents is then due to the relative dominance of the terms in equation (1)—we discuss this further in section 4.2.

[22] Figure 3a covers the LT band 09:45 to 10:32 h (hereafter the morning sector). The current density magnitude is largely invariant with latitude, though there are (rather indistinct) magnitude increases in both hemispheres from approximately $5°$ to $15°$ latitude (or the equivalent Southern Hemisphere latitude), which are likely related to the crests of the EIA. However, at this early LT, the EIA is not expected to have fully developed at CHAMP altitudes—this LT sector is included primarily to place the other sectors in better context. Since the morning sector shown here is recorded in Northern Hemisphere winter, we had anticipated the possible resolution of seasonal effects in the current density. *Balan and Bailey* [1995b] discuss seasonal effects on the EIA crest position, resulting from interhemispheric neutral wind flow in the thermosphere. Indeed, the magnitude of the relatively high-latitude current density estimates in this sector is increased in the Northern Hemisphere with respect to the Southern Hemisphere. However, this hemispheric difference in current magnitude is a nonseasonal effect, seen in each epoch covering the dayside. The hemispherical difference occurs in temporally adjacent epochs, between which the relative flight directions of the satellites will have reversed. Therefore, we are able to rule out relative satellite flight direction as its cause—it is likely due to the unavoidable inclusion of data affected by significant (interhemispheric) field-aligned currents in the satellite overflight calculation region. We see no current density trends which are attributable solely to season, in any epoch.

[23] Figure 3b covers the LT band 11:55 to 12:53 h (hereafter the noon sector). Just 2 h LT after the sector shown in Figure 3a, the plasma environment has changed significantly. As ionospheric plasma continues to rise in altitude, the magnitude of the current density estimates has increased, both near the equator and at higher latitudes. The changes at higher latitudes are obscured somewhat due to the limited latitude coverage of the sector shown in Figure 3a. However, epochs (not shown) between the LT sectors in Figures 3a and 3b show a consistent increase in magnitudes. In the noon sector, the bifurcated EIA crests between $10°$ and $20°$ latitude (and the equivalent negative latitudes in the Southern Hemisphere) are now clearer from the background scatter, indicating the development of the anomaly through LT.

[24] Results from the LT range 21:39 to 22:32 h (evening sector) are shown in Figure 3c. Several electrodynamic processes have taken place since the noon sector shown in Figure 3b. The EIA ascended to its full strength in late afternoon, continuing the trend of current density magnitudes increasing with LT throughout dayside. The PRE occurred about 3 h (LT) prior to this snapshot. In this evening sector, plasma production has mostly ceased and the EIA has begun to subside, although the reversal will not have substantially decreased the altitude of the *F* region yet. Despite the fact that the *F* region is near its peak altitude in this evening LT sector, presumably increasing plasma volumes at LEO altitudes, the current density estimates here show lower magnitudes than much of the dayside (though the magnitudes are comparable to those of the morning sector). We consider this apparent discrepancy to be a combination of two factors. First, *Balan and Bailey* [1995b] stated that the increased vertical plasma flow rate resulting from the PRE does not act to increase the amount of plasma in the *F* region, rather dispersing it to higher altitudes. If the decrease in plasma density at CHAMP altitude is greater than the increase at Ørsted altitude, the resolved current density will decrease. Second, the fact that this evening sector has a degree of scatter more similar to the results in Figure 3a than Figure 3d indicates that a continued driving force is affecting the currents. Therefore, the separate contributions to the total current density could be individually strong but could act to cancel out when summed, producing no obvious resultant trend in the data.

[25] As stated above, we cannot resolve individual sources of current contribution; however, some insight is possible from theory. *Maus and Lühr* [2006] showed that a gravity-driven current at LEO altitude encompasses this evening LT sector, having extrema at the EIA crest latitudes. The magnitude of the gravity-driven current in this sector is not greatly decreased from its dayside peak, corroborating the view that dayside-like magnitudes of current persist in the evening sector. The gravity current described by *Maus and Lühr* [2006] would cause wholly eastward current. Yet

in the estimates in Figure 3c, the EIA crests (with apparent peaks near latitudes of $\pm 15°$ QD latitude) show both westward and eastward current density increases. In addition to the pressure gradient and Lorentz contributions (mostly westward at this altitude) to the total current, *Alken et al.* [2011] discuss the effect of polarization electric fields (which create "feedback" currents via the electric Lorentz force) on the currents originally responsible for the polarization imbalance. This effect will be discussed further in section 4.2. In summary, a combination of the plasma dispersal related to the PRE, and opposing sources of current, appear to define the current density estimates in this LT sector.

[26] Figure 3d shows the LT range 02:26–03:14 h (post-midnight sector). At this LT, *F* region conductivity has decreased as the plasma descends into higher loss altitudes, and there is no direct electrodynamic driving force from the Sun. This is apparent in the greatly reduced near-equator scatter in the results compared with the morning, noon, and evening sectors. This nightside scatter reduction is typical across all epochs—where overlaps exist at the same UT and opposing LTs, the dayside values will always be "noisier." This suggests that the scatter seen on dayside is from an ionospheric rather than a magnetospheric origin. The low latitudes of this postmidnight sector are typified by lower magnitudes than on dayside. However, at higher latitudes (approximately $\pm 30°$–$50°$ magnetic latitude), there is a significant increase in current density. These midlatitude intensifications occur in each epoch with data after midnight, exhibiting both east and west current flow with typical peak magnitudes of ± 0.05 to 0.1 $\mu A/m^2$. This combination of latitude and LT is typically considered to be relatively free of currents, and the presence of these intensifications was not expected. The corresponding latitudes on dayside are free of this signal, with the exception of the afternoon sectors (not shown), which have typically strong values across a broad range of latitudes, but for which we have limited data coverage.

[27] We avoid claiming the discovery of a new ionospheric feature until the nightside midlatitude intensifications are resolved with an independent method (which is beyond the scope of this study) but, as for the rest of our data, we suggest several possibilities for the source of the observed trends. The high conductivity of the ionosphere in the direction of the magnetic field creates a "short circuit" along any magnetic field line, allowing electric fields to "map" to higher or lower altitudes than the region they were generated in *Rishbeth* [1988] and *Kelley* [2009]. A number of high-latitude/high-altitude processes affect the midlatitudes. The zonal current intensifications could be related to field-aligned currents from magnetospheric processes mapping down into the *F* region (discussed by *Rishbeth* [1971]), or a result of the transmission of electric fields and neutral winds from the auroral region to lower latitudes as discussed by *Heelis* [2004]. *Schunk and Nagy* [2009] discussed upflow of ionospheric plasma into the protonosphere (plasmasphere) during the daytime, and the subsequent descent of the plasma into midlatitudes at night. However, the limited coverage that we have in this epoch (and others in the same LT sector, not illustrated) depicts a signal in a narrow latitude band diminishing as the poles are approached, and latitudinal trends which do not correlate with *Dst*, implying a nonpolar, low-altitude origin

for the signal. The *F* region dynamo (and associated polarization fields) is a possible candidate for the cause of the midlatitude intensifications, but the intensification signal is not apparent south of $25°$ magnetic latitude—this could be explained by interhemispheric current flow along magnetic field lines. Assuming a dipole geometry, the altitude at the equator (apex altitude) of a specific field line is given by [*Campbell*, 2003]

$$a + p = (a + h)\sin^2(\theta_0),\qquad(7)$$

where *a* is the radius of the reference sphere (here 6371.2 km), *h* is the apex altitude (above this reference surface), and *p* and θ_0 are, respectively, the altitude and colatitude of an arbitrary observation point. From equation (7), field lines which enter the Earth's atmosphere at 400 km altitude and $25°$ magnetic latitude have apex altitudes of approximately 1870 km. The upper boundary of the conducting *F* region is somewhat diffuse, but it seems reasonable that field-aligned currents flowing between the two hemispheres in the $\pm 25°$ magnetic latitude range could offset any local charge imbalance, reducing the horizontal current flow. Above $25°$ magnetic latitude, the apex altitudes are likely to exceed the conducting part of the *F* region at this LT, preventing the (nonmagnetospheric) magnetic connectivity of the two hemispheres. This would lead to a local charge buildup and an associated increase in the horizontal current density. The suppression of the intensification signal at higher latitudes is likely due to decreasing conductivity as plasma density decreases away from the EIA. The likelihood of a poleward conductivity decrease suggests that transmission of electric fields between the poles and the midlatitudes would be difficult in this postmidnight LT sector.

4.2. Coupled Thermosphere-Ionosphere-Plasmasphere (CTIP) Comparisons

[28] We have assessed the likely electrodynamic fields behind the Ørsted/CHAMP estimates in each sector of LT and shown that, of the factors which can control the magnitude of our results (solar activity, geomagnetic activity, season, and longitude sector), none impacts on the trends we have discussed. However, we can only resolve the average current density and cannot distinguish between the separate contributing current sources in the satellite data. Hence, an independent validation of the broad-scale spatiotemporal trends in the Ørsted/CHAMP estimates is desirable. In this section, we compare our results to predictions of the Lorentz, gravity, and pressure gradient currents from the CTIP (Coupled Thermosphere-Ionosphere-Plasmasphere) model [*Millward et al.*, 1996]. CTIP is a self-consistent, first-principles, three-dimensional numerical model of ionospheric composition and temperatures. It is designed to highlight differences in small spatial-scale ionospheric dynamics between different geomagnetic activity conditions. Rather than relying on a parametrized electric field model for the low-latitude region, CTIP generates the low-latitude electric fields from the physics that determines the neutral winds, while the electron densities are determined from solar ionization. It is possible that in this process, the magnitudes of the electric fields and electron densities are being underestimated, and with them, the magnitude of the currents. By nature of its complete description of the relevant physics, we

expect CTIP to provide a better spatiotemporal representation of the currents than a smoothed empirical model could, but we should not expect an accurate match in terms of absolute values.

[29] The default output of CTIP is a series of latitude-longitude grids spaced vertically in terms of pressure. When pressure is converted to altitude, this spatial coverage does not usually extend to the altitude of LEO satellites (dependent to an extent upon modeled solar activity). In this study, we use the results from a special CTIP model run [*Lühr et al.*, 2008] in which the coverage was increased to 1000 km altitude. The extended data set is an hourly series of global 3-D output from CTIP covering a single day in July 2003, in which the $F_{10.7}$ solar flux density is fixed at 130×10^{-22} W/m^2/Hz. The challenge of increasing CTIP's coverage up to 1000 km altitude made production of more than a single day's extended output prohibitively difficult. In the following comparisons, we use the CTIP predictions to describe the distribution of the contributing current sources for a "quiet" ionosphere. This prevents the gravity- and pressure-gradient-driven contributions to the total current being overwhelmed by the Lorentz contribution. The trends discussed in section 4.1 are resistant to changes in *Dst* and solar flux, so a comparison with model values for a quiet ionosphere seems appropriate for identifying which current contributions are typically dominant in each LT sector (excepting periods of extreme geomagnetic or solar activity). The 3-D grid spacing of the extended CTIP output is 2° latitude, 18° longitude, and 50 km altitude (spanning 250 to 1000 km above a reference sphere of radius 6370 km). At each grid point, the atmospheric parameters output by CTIP were input into equation (1), and current densities from the gravity, pressure gradient, and Lorentz force contributions calculated. The first three spherical harmonic coefficients of the 2000 epoch in the 11th Generation International Geomagnetic Reference Field model [*Finlay et al.*, 2010] were used to compute the tilted-dipole ambient magnetic field estimate used in this process as CTIP does not support a more complex parametrization of the magnetic field.

[30] The zonal current density according to CTIP at 09:36 h LT is shown in Figure 4, with eastward currents again positive. The locations of the Ørsted (white) and CHAMP (black) overflights (for several hundred overflight calculation regions) are overlain for the morning LT sector (as shown in Figure 3b). The red box indicates a single overflight-calculation region for scale—the sides and top of this box are almost equal length in Cartesian coordinates. The altitude distribution of the overflights with regard to the EIA is clearly shown, though the anomaly has yet to fully bifurcate at this LT in the model. The Ørsted/CHAMP overflight locations vary both temporally and spatially, making sampling the CTIP values to the overflight locations difficult. We have applied a temporal simplification to the overflight locations, which occur in tightly clustered UT groups separated by a number of hours. The mean UT of each cluster of overflights is used in a 4-D interpolation to compute a new global 3-D grid of CTIP current density at the time of the overlap series. The new CTIP grids are each used in a trilinear spatial interpolation to sample CTIP current density predictions to the locations of the Ørsted and CHAMP satellite tracks. These samples are averaged over
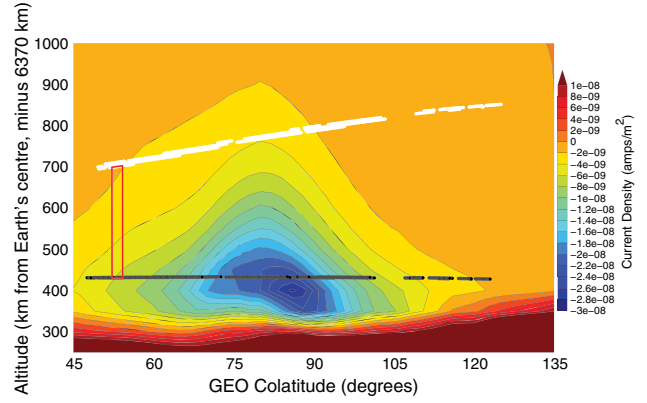

Figure 4. CTIP zonal current density prediction at a single local time of 09:30 h for a July day. Eastward flow is positive. The locations of several hundred Ørsted (white) and CHAMP (black) overflights are overlain for the local time sector 09:45 to 10:32 h. The LT range of this sector is slightly outside of the LT of the CTIP prediction shown, but since 09:30 is one of the LT grid nodes for CTIP, using this LT avoids the need for interpolation. The red box indicates a single overflight-calculation region for scale—the sides and top of this box are almost equal length in Cartesian coordinates.

the two altitude levels in each integral circuit, giving a single value per overflight for each force contribution to the zonal current density prediction.

[31] Figure 5 shows the same LT sectors as Figure 3, but with the Ørsted/CHAMP estimates smoothed (shown in black with a grey envelope of the nonsmoothed estimates), and the CTIP predictions overlain. The values cover the same latitude more than once because each 1 h wide band of LT contains results from about 15 days in UT (noncontinuous recording), and prior to smoothing, our estimates were grouped into clusters of similar UT. The blue points are the CTIP total zonal current density predictions, equal to the sum of the current contributions from gravity (green), pressure gradient (light blue), and Lorentz (magenta) forces. Note that the CTIP current densities have been (arbitrarily) multiplied by a uniform factor of 2 to aid in comparisons with the results from Ørsted and CHAMP. The CTIP prediction is typically an underestimate of the real data current density estimate magnitudes, implying that CTIP is perhaps over-effective at equalizing local divergence in the ionospheric electrodynamics. Though the magnitudes of the current density estimates differ between CTIP and the satellites, the spatiotemporal agreement shows several key similarities. The CTIP model prediction is dependent on the sum of several competing sources of current. Typically, where these sources diverge most strongly, the Ørsted/CHAMP estimates have their highest magnitudes. A notable exception to this is that the CTIP predictions in Figures 5a and 5b show the EIA in a nonbirfucated form, suggesting that the development of this structure is more rapid than is parametrized in the model. Despite these differences, it is notable that the magnitude offset between CTIP and the Ørsted/CHAMP estimates appears consistent between different LT sectors.

[32] In Figure 5a, there is a broadly similar latitudinal pattern to the magnitudes of the model predictions and Ørsted/CHAMP data estimates—a near-equatorial bulge
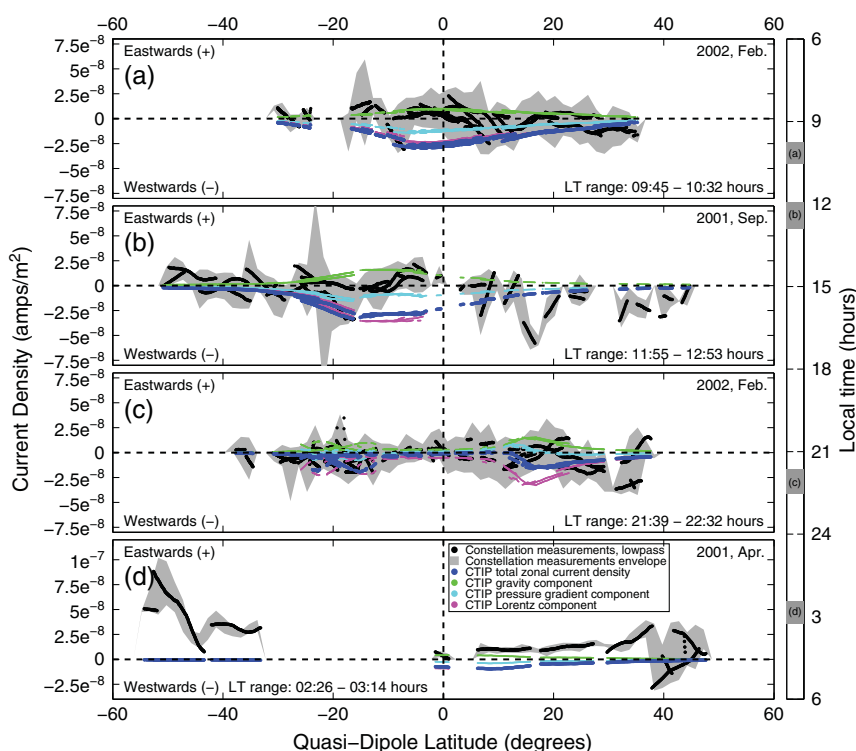
Figure 5. Comparison of CTIP predictions and Ørsted/CHAMP overflight estimates of current density. The subplots cover the same sectors of local time as Figure 3. The dark blue points are the CTIP predictions for total zonal current density sampled to the Ørsted and CHAMP locations, then averaged between the two different altitudes and multiplied by a constant factor of 2 to aid in comparisons with the satellite estimates. The modeled contributions of each force to the total zonal current density are shown as follows: green, gravity; light blue, pressure gradient; magenta, Lorentz. The sum of these contributions gives the dark blue points. The black points are the satellite data estimates from Figure 3, smoothed with a 50-point low-pass filter to remove the scatter and expose the underlying trends to aid comparison. The grey shading is a 1.5° latitude-smoothed envelope of the satellite estimates. The envelope was smoothed in the latitude coordinate frame, the black points in the UT frame. Eastward current flow is positive; westward negative.

with little extraneous signal at higher latitudes. However, the hemispherical difference in our current density estimates makes any more detailed comparison difficult, particularly at this early LT sector when the EIA has not fully developed. As noted above, the real data estimates appear to show a more bifurcated EIA than the CTIP prediction does.

[33] While in Figure 5b, the CTIP predictions appear not to have increased in magnitude (from the previous LT sector) in line with the Ørsted/CHAMP data estimates, this is likely due to a decreased plasma pressure gradient contribution and an increased gravity current contribution, affecting the resultant total magnitude of the prediction. The latitude of the CTIP peak magnitude in this sector is in the Southern Hemisphere since the CTIP prediction is for Northern Hemisphere summer, while our estimates in this sector are for the equinox. Note that the magnitude peak in the Ørsted/CHAMP data estimates between 5° and 20° QD latitude—this is thought to be due to the EIA crest. If this is true, then regardless of the season of the CTIP prediction, the model again appears to have insufficient EIA bifurcation in this LT sector.

[34] In Figure 5c, the CTIP values show a magnitude decrease in line with the decrease in the Ørsted/CHAMP data estimates from dayside LT sectors. In this evening

sector, the EIA crest positions in the data estimates and the model prediction appear in much better agreement than on the dayside, though this is less clear in the Northern Hemisphere. The cause of the Northern Hemisphere intensifications in the Ørsted/CHAMP data estimates at higher latitudes is unclear—they could be related to bias from FACs, or could be related to the midlatitude intensifications seen more clearly in the postmidnight sector. CTIP does not predict them, for which we offer reasons in the next sector's analysis.

[35] In Figure 5d, both data and model show a marked decrease in near-equatorial magnitudes, though the agreement worsens at higher latitudes. Without direct ionizing irradiation from the Sun, the nightside *F* region is subject to a different balance of controlling forces than the dayside and can exhibit mesoscale structure which would not be dominant during sunlit hours [*Kelley*, 2009]. Although the dayside is host to stronger currents with an associated higher error in their prediction, the nightside ionosphere is considered more challenging to parametrize effectively than the dayside because the dominant forcings are more difficult to predict. CTIP has evidently not parametrized the midlatitude intensification signal—we suggested earlier that these intensifications could be due to the inability of the midlatitudes to
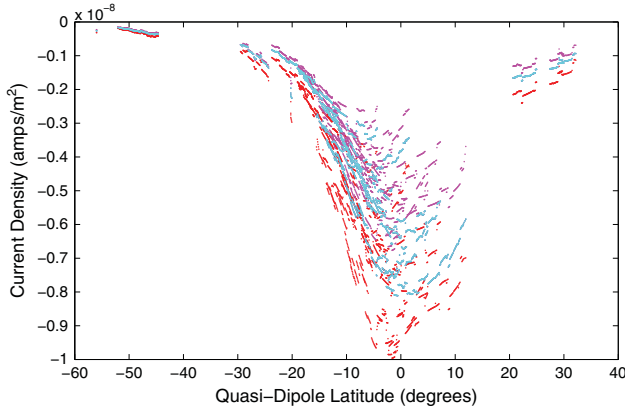
Figure 6. Values of input and recovered synthetic current density model prediction data for a series of overlaps at the same LT. The input values of current density prediction means for the sparse and dense integral loops (explained in the main text) are shown as red and dark blue points, respectively. Note that the dark blue points are obscured by the light blue points. The magenta and light blue points are the recovered current density mean values for the sparse and dense loops, respectively. The proportional recovery is shown in Figure 7.

connect via field-aligned currents at this LT. A parametrization simplification adopted by CTIP, intended to force the global mean divergence in the currents to zero, closes the horizontal currents via field-aligned currents. It could be that this simplification is preventing the appearance of the midlatitude intensifications in CTIP's prediction.

[36] The CTIP comparisons use a single day of data prediction made with fixed values for solar activity and season (representing Northern Hemisphere summer, moderate solar flux, and quiet geomagnetic conditions). At higher geomagnetic activity levels, the contributions from the gravity and pressure gradient forces will cease to affect the Lorentz contribution significantly. The balance of contribution values to CTIP's total zonal current density shown here will not be applicable in all conditions. Despite this simplification, the comparisons have been instructive in assessing the input of each current type into the bulk signal typical for a "quiet" ionosphere, as well as validating the spatiotemporal trends in our results.

4.3. Assumption of Vertical Current Trends Across Calculation Region

[37] In section 3, we made the assumption of current density varying linearly with altitude throughout the calculation region. The altitude distribution of the current density predicted by CTIP is shown in Figure 4. Rather than varying linearly between the two satellites' orbits, the falloff of the current density with altitude is approximately exponential. Our current density estimates are thus biased from the real-world case by an amount equivalent to the difference between the real gradient in the current density across the calculation region, and the assumed linear gradient. We have constructed a synthetic test of input and recovered model values of current density to illustrate the degree of bias this simplification imposes, which we summarize here.

[38] The data used in the synthetic recovery test are the Ørsted and CHAMP measurement positions for the satellite data arcs in a series of overlap locations (those in the green box in Figure D1). There are over 3000 overlaps in this set of data, each of which (initially) comprises an arc of Ørsted data 2° colatitude in length, and the same for CHAMP. For each overlap, two integral loops of location data are constructed. The first loop is simply the positions of the satellite data comprising the overlap, with no measurement locations on the radial line elements—this is termed a "sparse" loop. For the second loop, the mean sampling interval of the Ørsted and CHAMP measurements is used to synthesize a series of "measurement positions" along the radial line elements of the sparse integral loop. The combination of the sparse loop and these new data positions is termed the "dense" loop, intended to represent an idealized data distribution for the integral.

[39] We sampled 3-D CTIP current density values to each of the data positions in the 3000+ sparse and dense loops. For each loop, the mean current density in the direction normal to the plane enclosed by the integral loop was calculated—sparse loops have a slightly higher mean current density than dense loops due to the aforementioned nonlinear falloff in current density with altitude. The mean current densities were used to calculate the synthetic current I_{syn} enclosed in each integral loop by multiplying the appropriate mean current density by the area enclosed in the integral loop. This area was calculated from a summation of the triangular area elements of the sparse loops, as given by equation (B1). The enclosed area is identical for the sparse and dense loops. The synthetic current (sparse/dense, respectively) is then used to calculate its magnetic effect at each of the sparse and dense loop data locations via an application of the Biot-Savart law [*Fleisch*, 2008]

$$\mathbf{B}_{syn} = \frac{\mu_0 I_{syn}}{2\pi r} \hat{\mathbf{s}}, \tag{8}$$

where $\mathbf{B}_{syn}$ is the magnetic effect (at a certain location) of the enclosed synthetic current I_{syn}, μ_0 is the permeability of free space, $\hat{\mathbf{s}}$ is a unit vector in the direction of the magnetic field which results from a current flowing through an infinite length thin wire at the center of the integral loop, aligned in the direction normal to the plane of the enclosed area, and r is the length of a vector connecting the center of the integral loop to the point at which $\mathbf{B}_{syn}$ is predicted. This application of the Biot-Savart law (as well as the previous step of taking the mean current density for the integral loop) reduces the original 3-D current density distribution to a mean scalar value. This is the same simplification implicit in our application of the integration method used to resolve current density from the real data, so the errors resolved in this test should be similar to those encountered in the real data. $\mathbf{B}_{syn}$ is the synthetic data equivalent of $\Delta \mathbf{B}$ in equation (4), and thus the line elements, along-track rotation, enclosed area, and resulting recovered synthetic current density are calculated via the process described for the real data in section 3 and the appendices.

[40] The input and recovered current density values for the sparse and dense loops are shown in Figure 6. The input values for the dense loops are obscured by the dense loop recovery values, since their retrieval proportion is near 100%. Figure 7 shows the proportional recovery in more
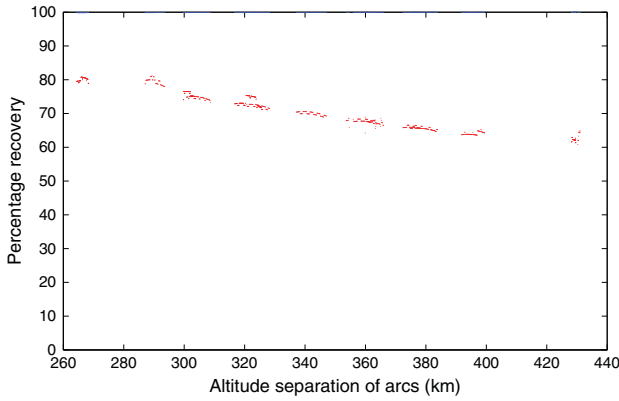
Figure 7. Percentage recovery of synthetic current density model prediction data for a series of overlaps at the same LT, shown plotted against the altitude separation of the two satellites. Red points are the percentage recovery for sparse integral loops, blue for dense loops (the terms "sparse" and "dense" are explained in the main text). The dense loop recovery values do not drop below 99.98%. The sparse loop recovery varies between 80% and 60%, dependent upon the altitude separation of the Ørsted and CHAMP satellites. The range of altitude spans shown is representative of the full extent of altitude spans seen in the real data.

detail. The sparse loop recovery proportion varies between 80% and 60%, dependent upon the altitude separation of the Ørsted and CHAMP satellites. The sparse loop recovery is considered representative of the case for the real data, and the estimates presented in section 4.1 are assumed to be slight underestimates of the real case. However, as stated in section 3, this does not affect our interpretation of the current density trends, which are considered robust. In addition to the discussion of vertical current density trends here, we note that the horizontal variation in the current density (shown in Figure 4) across the calculation region (2° colatitude) is negligible, and the along-orbit propagation of the integral region should offset any errors resulting from horizontal gradients in the current distribution. The assumptions in our model do not invalidate the results, as long as these limitations are borne in mind when drawing conclusions from them.

5. Conclusions

[41] We have demonstrated a robust method of resolving zonal current density on an event-by-event basis at LEO altitudes using satellite magnetic data. The use of multiple satellites minimizes the contribution of magnetic fields outside the calculation region to the resolved current density, since no assumptions about current geometry or stationarity are required. Ampère's integral is able to provide useful information about current flow at LEO satellite altitude, within the framework of the biases already stated. The data provided by this application of Ampère's integral span all local times twice, but we cannot use this data set by itself to provide a consistent global representation of the currents. At any one overlap, the factors of satellite altitude, season, solar flux, missing data, and distribution in colatitude all combine to disrupt any trend that might otherwise be coherent in local time. Despite this, our results largely mirror the EIA

cycle and appear resistant to the other factors affecting each overlap. The currents also appear unmodulated at times of either high-negative Dst or high $F_{10.7}$. This has implications for any future efforts to model the effect of these currents and indicates that their generation is primarily associated with a steady diurnal pattern of atmospheric plasma generation and transport. We see higher magnitudes of current density in the dayside equatorial regions, the result of Ørsted, and CHAMP passing through the EIA in colatitude as the two satellites cross in local time. After midnight, once the peak density of the EIA has descended appreciably in altitude on nightside, we resolve significantly lower equatorial current densities with greatly reduced scatter. The midlatitudes of the nightside local time sector are typically considered free of electric currents, yet here we consistently resolve a series of zonal current density intensifications. The causes of these unexpected intensifications remain an open issue—we suggest caution when using only nightside data in geomagnetic field modeling, as our results indicate that it may not be as free of electric currents as is usually assumed.

[42] A comparison of the satellite measurements with CTIP current density predictions shows reasonable spatiotemporal agreement on the dayside, with both data sets consistently exhibiting strong westward current flow at LEO altitude. The agreement on nightside is poorer, but both data sets show a significant magnitude reduction relative to dayside. CTIP has shed light on the balance of forces contributing to the total zonal current density, confirming that the EIA signal remains strong several hours into the nightside even though the measured total zonal current density does not reflect this. Most striking in these comparisons is the high magnitude of the satellite estimates relative to CTIP, though the agreement with existing estimates of current density [e.g., *Olsen*, 1997] is within expectations. Identifying the ionospheric physics behind this magnitude difference is beyond the scope of this paper. However, the interested reader is referred to *Alken et al.* [2011] for a discussion on a possible cause of the pressure gradient current's high strength, and to *Kelley* [2009], and *Schunk and Nagy* [2009] for a discussion on the competing electrodynamic influences in the F region.

[43] An improved description of radial ionospheric electrodynamics requires a more complete data set. ESA's upcoming mission *Swarm* (described in *Olsen et al.* [2007]), with its upper satellite at an altitude of 530 km and its two lower satellites at an altitude of (initially) 450 km, has an ideal vertical distribution for an independent resolution of these currents. However, after the initial launch of the satellites in the same orbital plane, the upper and lower satellites do not occupy similar local times for another 3.5 years. This may be after the atmospheric re-entry of the lower pair of satellites. If the Swarm satellites do achieve more than a single series of crossovers, they will provide a more detailed altitude profile of the currents than the Ørsted/CHAMP configuration, but at a limited series of local times.

Appendix A: Rotation to the Along-Track Coordinate Frame

[44] The value of Ampère's integral (equation (2)) is dependent on the direction defined by the geometry of the satellites' overflight—we express this direction in the

geographic (GEO) system (defined in section 2). The calculation of the contribution of each line element (each successive pair of points) to the integral sum is applied in the along-track coordinate frame. *Ritter and Lühr* [2006] applied a similar process, treating each instantaneous "quad" of measurement points as a locally horizontal surface. However, Ørsted and CHAMP both have slight (and differing) inclinations away from exactly-polar orbits, so our calculation region is a skew quadrilateral [*Weisstein*, 2003] rather than a flat plane. As either Ørsted or CHAMP approaches the geographic pole, the inclination of the orbit results in a deviation between the geographic zonal direction and the strike-flight direction. The effect of this is to make the integral loops less zonally-facing (i.e., less parallel to a meridional line) at higher latitudes, and we have restricted our analyses to lower latitudes for this reason. The use of an along-track calculation frame for each pair of points around the integral circuit ensures that the coordinate frame in which the solution is expressed is the one which best fits each overflight's geometry. Here we describe the process of rotating the magnetic vector into the along-track frame.

[45] For the two magnetic vectors associated with each line element, we seek the component of each in the direction of integration. The conversion from GEO (the frame in which we identify overlap instances) to the along-track coordinate frame takes the form of three spherical rotations in the Cartesian frame. Therefore, we start this process with $\mathbf{dl}$ (equation (3)) and $\Delta\mathbf{B}$ (equation (4)) in the Cartesian frame (using the transformations described by, e.g., *Hapgood* [1992] and *Langel and Hinze* [1998]). We use the Cartesian components (x, y, and z) of $\mathbf{dl}$ to define the rotation process, which we in turn apply to $\Delta\mathbf{B}$. The along-track direction has been defined such that when $\mathbf{dl}$ is rotated to $\mathbf{dl}_{AT}$ in the along-track frame, its x component will point directly along-track. The transformation matrices for spherical rotations in the Cartesian frame about each of the principal axes are given here. For ease of reference, we will later refer to these in terms of the rotation angle and the principal axis as follows: a rotation about the x axis by an angle of α is given as $\langle\alpha,X\rangle$.

[46] We operate in a right-handed coordinate system [*Boas*, 2006] and the rotation matrices shown below will rotate in an anticlockwise direction for a positive angle, if our viewpoint is on the positive part of the stationary axis, facing toward its origin. The rotation matrices for each of the three axes are the following:

$$\langle\alpha,X\rangle = \begin{pmatrix} 1 & 0 & 0 \\ 0 & \cos\alpha & \sin\alpha \\ 0 & -\sin\alpha & \cos\alpha \end{pmatrix}$$

$$\langle\alpha,Y\rangle = \begin{pmatrix} \cos\alpha & 0 & -\sin\alpha \\ 0 & 1 & 0 \\ \sin\alpha & 0 & \cos\alpha \end{pmatrix} \quad \text{(A1)}$$

$$\langle\alpha,Z\rangle = \begin{pmatrix} \cos\alpha & \sin\alpha & 0 \\ -\sin\alpha & \cos\alpha & 0 \\ 0 & 0 & 1 \end{pmatrix}.$$

[47] Rotation 1: rotate the x, y plane about z until the x' axis points through the meridian of the first of the two points which make up $\mathbf{dl}$. Calculation of the rotation angle α_1 is applied in the x, y plane, assuming conversion from radians

to degrees, and correcting for quadrant as follows:

$$\alpha_1 = \begin{cases} \tan^{-1}\left(\frac{y_1}{x_1}\right) + 180 & \text{if } x_1 < 0 \\ \tan^{-1}\left(\frac{y_1}{x_1}\right), & \text{otherwise.} \end{cases} \quad \text{(A2)}$$

The new coordinate system is calculated via

$$\begin{pmatrix} x' \\ y' \\ z' \end{pmatrix} = \langle\alpha_1, Z\rangle \begin{pmatrix} x \\ y \\ z \end{pmatrix}. \quad \text{(A3)}$$

[48] Rotation 2: rotate the x', z' plane about y' until the x'', y'' plane is parallel to $\mathbf{dl}'$, and the first of the two points of $\mathbf{dl}'$ is at zero on the x'' axis:

$$\alpha_2 = \begin{cases} -\tan^{-1}\left(\frac{z_2'-z_1'}{x_2'-x_1'}\right) + 180 & \text{if } x_2' - x_1' < 0 \\ -\tan^{-1}\left(\frac{z_2'-z_1'}{x_2'-x_1'}\right), & \text{otherwise.} \end{cases} \quad \text{(A4)}$$

Then

$$\begin{pmatrix} x'' \\ y'' \\ z'' \end{pmatrix} = \langle\alpha_2, Y\rangle \begin{pmatrix} x' \\ y' \\ z' \end{pmatrix}. \quad \text{(A5)}$$

[49] Rotation 3: rotate the x'', y'' plane about the z'' axis to put the x''' axis in line with both the points making up $\mathbf{dl}''$. If the second rotation was applied correctly, this angle should not have to exceed 180° but we include the quadrant correction for completeness.

$$\alpha_3 = \begin{cases} \tan^{-1}\left(\frac{y_2''-y_1''}{x_2''-x_1''}\right) + 180 & \text{if } x_2'' - x_1'' < 0 \\ \tan^{-1}\left(\frac{y_2''-y_1''}{x_2''-x_1''}\right), & \text{otherwise.} \end{cases} \quad \text{(A6)}$$

Finally,

$$\begin{pmatrix} x''' \\ y''' \\ z''' \end{pmatrix} = \langle\alpha_3, Z\rangle \begin{pmatrix} x'' \\ y'' \\ z'' \end{pmatrix}. \quad \text{(A7)}$$

$\mathbf{dl}_{AT}$ is then $\mathbf{dl}'''$. The full rotation matrix R from GEO to the along-track frame is

$$R = \langle\alpha_3, Z\rangle \langle\alpha_2, Y\rangle \langle\alpha_1, Z\rangle. \quad \text{(A8)}$$

We must rotate the location coordinates at each of the previous three stages, since the angle calculations require this intermediary information. However, we may apply R to the magnetic perturbation vectors in one step to derive

$$\begin{pmatrix} \Delta B_{ATx} \\ \Delta B_{ATy} \\ \Delta B_{ATz} \end{pmatrix} = R \begin{pmatrix} \Delta B_x \\ \Delta B_y \\ \Delta B_z \end{pmatrix}. \quad \text{(A9)}$$

[50] The along-track component for each of the magnetic perturbation vectors is now their respective x components.

Appendix B: Calculation of the Integral Circuit's Bounded Surface Area

[51] To calculate the area enclosed by the Ørsted and CHAMP arcs, we define a series of meshing triangles in the Cartesian frame, each comprising two locations from one arc (the baseline) and the third from the other arc. The baseline arc is switched for the next triangle in the mesh. The

Table C1. Invalid-Solution Rejection Criteria

Parameter	Rejection Value	Justification
LT difference between arcs	> 0.096 h (5.75 min)	> 4× time span of Ørsted arc
| Arc length |	> 10% of 2° colatitude	N/A
Max |$\mathbf{dl}$|	> max satellite altitude difference	N/A
Min |$\mathbf{dl}$|	|$\mathbf{dl}$| < 4 km or |$\mathbf{dl}$| > 8 km	To identify geometrical errors
Loop surface area	> ±15% of expected value	Indicates area selection error
Loop surface normal unit vector	θ component > 0.14	Empirical, greater at high latitudes
% missing points in integral loop	> 15%	Empirical (tested with synthetic data)
Magnetic colatitude	Within 40° of geomagnetic poles	Avoiding auroral regions
UT difference between arcs	> 0.096 h	> 4× trace time of Ørsted arc
ϕ span between arcs	> 4°	Empirical (tested with synthetic data)

area A of each triangle is calculated via Heron's formula [*Dunham*, 1990]

$$sl_1 = \sqrt{(bl_{1x} - bl_{2x})^2 + (bl_{1y} - bl_{2y})^2 + (bl_{1z} - bl_{2z})^2}$$

$$sl_2 = \sqrt{(bl_{2x} - t_x)^2 + (bl_{2y} - t_y)^2 + (bl_{2z} - t_z)^2}$$

$$sl_3 = \sqrt{(t_x - bl_{1x})^2 + (t_y - bl_{1y})^2 + (t_z - bl_{1z})^2}$$

(B1)

$$p = (sl_1 + sl_2 + sl_3)/2$$

$$A = \sqrt{p \cdot (p - sl_1) \cdot (p - sl_2) \cdot (p - sl_3)},$$

where sl_{1-3} are the triangle side lengths, bl indicates the two baseline points (with the subscripts 1 and 2 used as in section 3), t indicates the third point in the triangle, and p is the semiperimeter of the triangle. The total area is the sum of the contributions A. This method is resilient to errors resulting from missing data since the baseline is a good approximation to a tangent for the satellite path, and remains so even if several points are missing. If either satellite arc has more points than the other arc, it is used as a series of baselines with the third point provided by the end point of the shorter arc until all the locations in the calculation region have been accounted for.

Appendix C: Table of Rejection Criteria

[52] As stated in section 3, the initial criteria used to reject nonoverlapping Ørsted and CHAMP data were too accommodating. Table C1 shortlists and justifies the entire set of rejection criteria used to produce the results in this study. These have been verified with the synthetic *Swarm* data produced by *Olsen et al.* [2007].

Appendix D: Sources of Error and Uncertainty

[53] While our results originate from individual crossovers of the satellites, they are not direct measurements. Compared to the magnitude of the full geomagnetic field, we are isolating a relatively small signal from much large background trends. A discussion of possible sources of error follows. Figure D1 shows the distribution of our estimates in local time. The values highlighted in the boxes will be discussed in the following sections.

D1. Temporal Lag Permitted in Integral Loop

[54] Part of the appeal of studying low latitudes is that the response times of the current distributions to electrodynamic forcing are large compared to the time taken to complete an overflight. For this reason, we have not allowed for changing electric flux in equation (2) (doing so would make this the Ampère-Maxwell law). However, the signals from the magnetospheric magnetic fields are highly time variant. The overflights are near-simultaneous, but not precisely so. The propagation along-orbit increases this difference, especially when the satellites' orbits are in different directions. Any temporal offset between the two contributing tracks in the integral loop will have associated different measurements of the magnetospheric fields. This will act as a source of noise in the data. Here we assess the severity of this effect on our estimates.

[55] The mean time taken by Ørsted and CHAMP to trace a 2° long arc is roughly 30 s. The results shown in Figure D1 (and elsewhere throughout this manuscript unless stated otherwise) have been allowed a time difference between the mean LTs of each arc of up to ±5.75 min (likewise for the mean UT difference). Therefore, the time difference between the arcs can be more that 5 min greater than the time taken to record the data for a single arc. The temporal lag allowed between the arcs is generous in order to increase
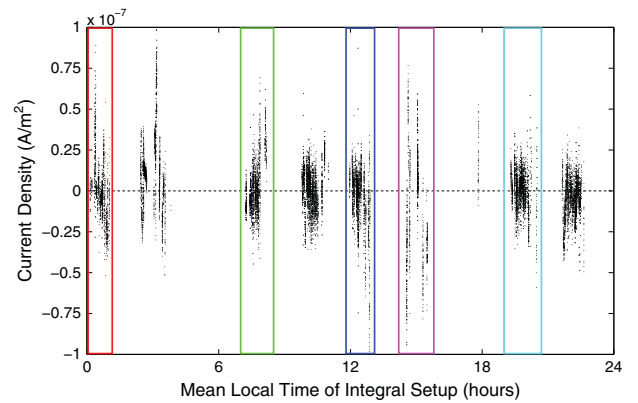

Figure D1. Current density versus distribution of Ørsted and CHAMP overlaps for all LTs. The EIA-related trends here are scattered due to the interference of several dependencies in the results. Here we highlight the "boxed" sets of values: the red and dark blue boxes show a pair of current density estimates from data recorded at the same UT, and the light blue/green boxes show a different set of results from an identical UT (though this is different to the UT of the other boxed values). These will be discussed later, in relation to Figures D5 to D8. The values in the magenta box will also be discussed below, in relation to Figure D3.
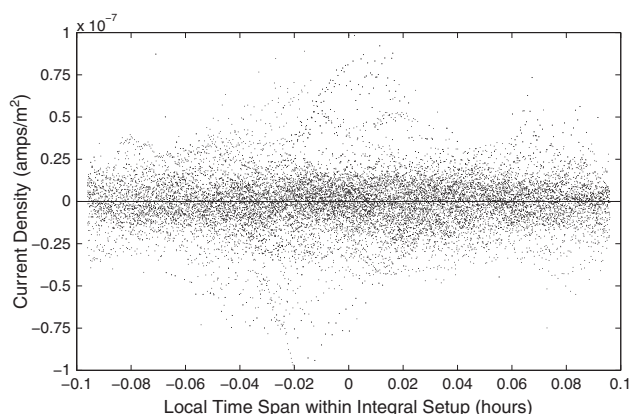
Figure D2. Local time difference within calculation region. Each point is the mean local time of the Ørsted arc minus that of the CHAMP arc. The *x* axis spans the time interval (±5.75 min) between local times allowed in the calculations shown in Figure D1. The scatter is laterally uniform across the chart, indicating that the calculation method we use produces equally reliable results throughout the time taken to record a full loop of data from the two satellites.

data coverage. Here we examine the effect of changing the time difference cutoff. The trend for variation in solution value with increasing LT gap is shown in Figure D2, which spans ±5.75 min (0.096 h) on the abscissa. We point to the lack of difference in lateral trend in this chart as good evidence that the calculation method is temporally steady, for as far as can be resolved in time without incurring overflight-geometry-based errors in the solutions. However, this does not account for LT-dependent effects. In Figure D3, we show the data from Figure D1 with the allowed time gap reduced to just over 1 min (the ±0.02 h span in Figure D2). Note that the magnitude of the boxed values does not differ significantly from Figure D1. We surmise that the temporal error
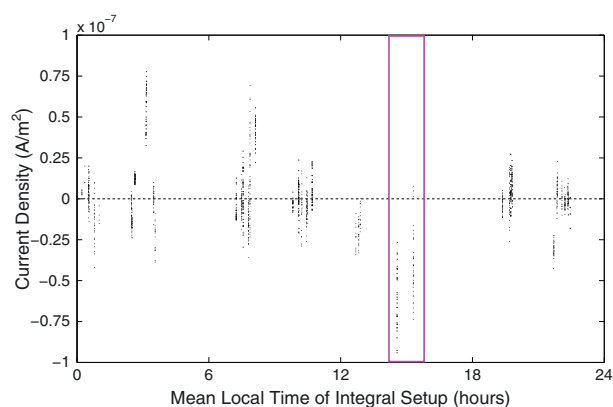

Figure D3. Current density versus distribution of Ørsted and CHAMP overlaps for all local times. Identical to Figure D1, except that the allowed mean time gap (in local time) between the contributing arcs has been decreased from 0.096 h (5.76 min) to 0.02 h (1.2 min). Note that the amplitude of the highest-magnitude results (boxed) is not diminished by this step.
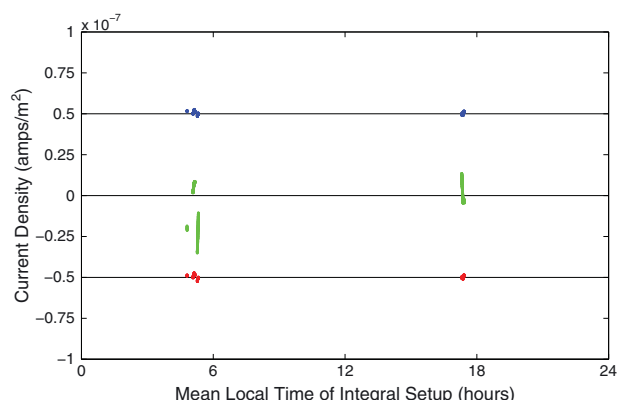
Figure D4. Simulated *Swarm* data: solutions for zonal current density. The distribution of *Swarm* overlaps between the upper and (one of the) lower satellites in local time versus current density is repeated three times, with arbitrary vertical offsets for clarity. The ordinate scale is identical to that of Figure D1 for ease of comparison. The blue data show the unedited solutions, exhibiting minimal current density. The red data show solutions from the same overlap series, with an error of 10 arc sec applied to the first Euler angle of the lower satellite—the effect on the solution is minimal. The green data again show solutions from the same overlap series, with an error of 431 arc sec applied to the first Euler angle of the lower satellite—the effect is appreciable. The three black lines are zero-lines of current density for each of the three series.

imposed by our choice of arc length does not significantly affect the solutions.

D2. Effect of Attitude Error

[56] The rotation of satellite magnetic data from the frame of the vector fluxgate magnetometer (VFM) to an Earth-centered, Earth-fixed (ECEF) frame involves an in-flight estimation of the three Euler rotation angles [*Olsen et al.*, 2007]. These are estimated under the assumption that the currents described in this paper do not exist. It is possible that the rotation process could screen out the signal we are attempting to resolve. Worse, the results of the integral could simply be due to attitude offsets between the Ørsted and CHAMP satellites. Here we assess the likelihood of this occurring.

[57] Simulated data from the ESA's upcoming mission *Swarm*—described in the End-to-End mission simulator study [*Olsen et al.*, 2007]—were used to calculate Ampère's integral in an identical manner to the actual data from the Ørsted and CHAMP satellites. Since the simulated *Swarm* data are all based on potential fields, we expect zero current density except for errors introduced by time differences within the integral setup. The blue points in Figure D4 show the *Swarm* integral solutions, with an arbitrary vertical offset applied to aid comparison with the following data series.

[58] The Ørsted and CHAMP Euler rotations are determined to better than 20 arc sec, equivalent to a combined magnetic error of around 5 nT in a 50,000 nT ambient field. The red points in Figure D4 show that the result of directly applying a 10 arc sec attitude error to the first Euler angle (for the lower satellite only) used in the VFM-ECEF rotation
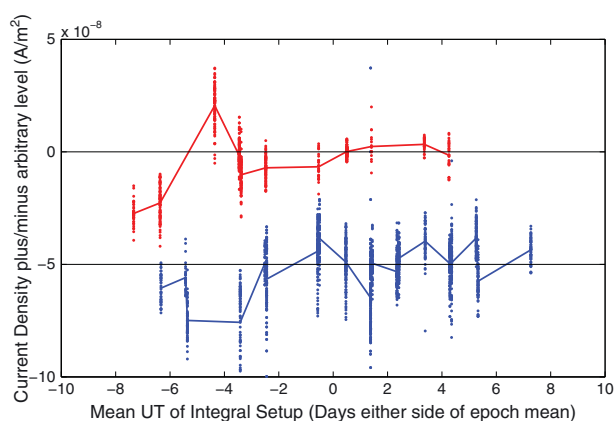
Figure D5. Comparison of current density estimates made at the same UT, shown in the red and dark blue colored boxes in Figure D1 (the colors here are as per the colors of the boxes). The blue colored values have been shifted in the negative direction by 0.05 μA/m^2 in order to distinguish the two data sets: the black "zero" lines are at levels of 0 and −0.05 μA/m^2 for red and blue sets, respectively. A line has been traced through the mean of each cluster of values to highlight the trends in UT. A comparison of the shared UT trends in relation to the trends in Figure D7 (which shows radial line element length discrepancy) is made in the main text. In summary, since this set of overlaps shows no effect from Euler angle estimation, and a superficial similarity to the UT trends in the radial line element length discrepancy, the error from both these factors is likely minimal.

Figure D6. Comparison of current density estimates made at the same UT, shown in the green and light blue colored boxes in Figure D1 (the colors here are as per the colors of the boxes). The blue colored values have been shifted in the negative direction by 0.05 μA/m^2 in order to distinguish the two data sets: the black "zero" lines are at levels of 0 and −0.05 μA/m^2 for green and blue sets, respectively. A line has been traced through the mean of each cluster of values to highlight the trends in UT. A comparison of the shared UT trends in relation to the trends in Figure D8 (which shows radial line element length discrepancy) is made in the main text. In summary, this set of overlaps shows a strong impact from the Euler angle estimation process but shows no similarity to the UT trends in the radial line element length discrepancy.

is minimal—this is also the case for 10 arc sec errors applied to the second and third Euler angles (results not shown). Note that the red points have been vertically shifted in an opposite manner to the blue points for clarity.

[59] Testing this effect further, we applied an extreme attitude error to the first Euler angle, changing the rotation by 431 arc sec, equivalent to 25% of the total rotation amount. The results, demonstrating an appreciable effect, are shown by the green points in Figure D4. Hence, to mimic the magnitude of the current densities obtained with Ørsted and CHAMP, we require the application of unrealistic attitude errors. From this, we infer that typically occurring attitude errors will have no effect on our results.

[60] While we have ruled out the possibility of attitude error directly causing the magnitude of current densities estimated, it does not preclude the possibility of the currents being "screened out" by the Euler angle estimation process, since this occurs in-flight. Convention for the timescale of this estimation differs but is typically on the scale of at least a day. The Ørsted and CHAMP overlaps occur on each "side" of the Earth at the same UT. We can therefore look at integral solutions which are similar in UT but separated in LT to assess the effect of the Euler angle estimation.

[61] Figure D5 shows the two sets of values in the red and dark blue boxes in Figure D1 (the colors here are as per the colors of the boxes). Here they are distributed in UT, with an arbitrary vertical offset of −0.05 μA/m^2 applied to the blue points to distinguish the two sets. A line has been traced through the mean of each cluster of values to show the trends in UT. Both red and blue sets show a broad trend for values
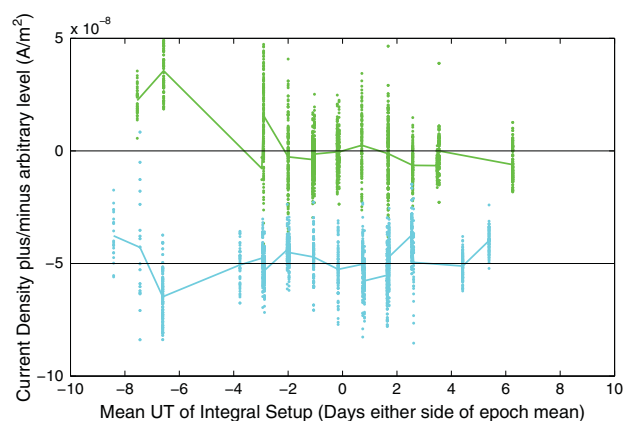
increasing with UT. Each cluster of values occurs within a few minutes of UT, so if the Euler angle estimation was affecting these values, a "mirrored" trend (opposite in sign for each opposing LT) would be seen in their UT progression. No such trend is seen in this example, but this is not the
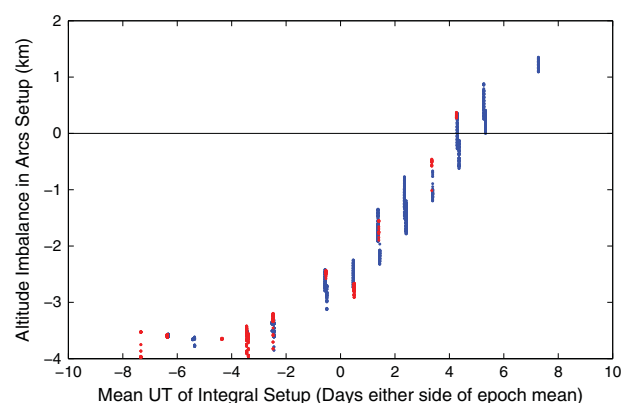

Figure D7. Radial line element length discrepancy in units of kilometer, for overlaps in the red and dark blue boxes in Figure D1 (the colors here are as per the colors of the boxes). Each point is the difference between the radial line element lengths in each integral loop. The two trends in UT here are very similar and bear a superficial similarity to the UT trends in Figure D5. Further analysis of the trends is given in the main text.
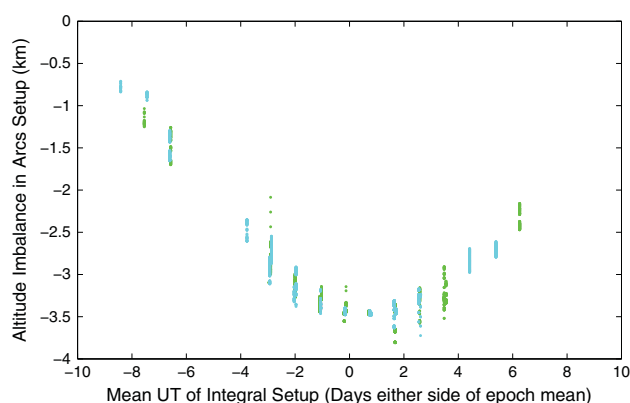
Figure D8. Radial line element length discrepancy in units of kilometer, for overlaps in the green and light blue boxes in Figure D1 (the colors here are as per the colors of the boxes). Each point is the difference between the radial line element lengths in each integral loop. The two trends in UT here are very similar but bear no similarity to the UT trends in Figure D6. Further analysis of the trends is given in the main text—in summary, a discrepancy in the lengths of the radial line elements does not affect the estimation of current density.

case for all epochs. Figure D6 shows the two sets of values in the green and light blue boxes in Figure D1, in a similar layout to Figure D5. This set of overflights does appear to be affected by the Euler angle estimation. In the set of overflights shown in Figure D6, it is not possible to separate which of the two LTs the current density trends stem from as the magnitudes are split evenly between both opposing LTs. Fortunately, most sets of overflights appear unaffected by the Euler angle rotation process, and in this paper, we have only analyzed current density estimates from LT sectors which do not exhibit this aliasing effect.

D3. Effect of Satellite Altitude Changes Within the Integral Calculation Region

[62] In the integral loop, the longest line elements are the radial lines connecting the Ørsted and CHAMP arc edges. We treat the magnetic difference across this gap in the same manner as that across any of the other line elements in the circuit. Any difference in the length of the two radial line elements could lead to a multiplication effect in the net magnetic difference, biasing the integral summation. Here we assess this effect using the same two sets of values as shown earlier in Figures D5 and D6.

[63] The UT trends in the radial line element length discrepancy for the two sets of data in Figure D7 are nearly identical. While the slope of the UT trend in Figure D7 appears superficially similar to the UT trend in the current density estimates shown in Figure D5, note that the trends in the radial line element length discrepancy are nearly maximal at the UT of 0, whereas the same is not true for the current density estimates. The two UT trends in radial line element length discrepancy shown in Figure D8 are also very similar to each other. The same is not true of the current density estimates for the same data, shown in Figure D6. These results indicate that a discrepancy in the lengths of the radial line elements does not appear to affect the estimation of current density.

References

Alken, P., and S. Maus (2010), Electric fields in the equatorial ionosphere derived from CHAMP satellite magnetic field measurements, *J. Atmos. Sol. Terr. Phys.*, *72*(4), 319–326.

Alken, P., S. Maus, A. D. Richmond, and A. Maute (2011), The ionospheric gravity and diamagnetic current systems, *J. Geophys. Res.*, *116*, A12316, doi:10.1029/2011JA017126.

Amm, O., R. Fujii, K. Kauristie, A. Aikio, A. Yoshikawa, A. Ieda, and H. Vanhamki (2011), A statistical investigation of the Cowling channel efficiency in the auroral zone, *J. Geophys. Res.*, *116*, A02304, doi:10.1029/2010JA015988.

Appleton, E. V. (1946), Two anomalies in the ionosphere, *Nature*, *157* (3995), 691–691.

Bailey, G. J., N. Balan, and Y. Z. Su (1997), The Sheffield University plasmasphere ionosphere model—A review, *J. Atmos. Sol. Terr. Phys.*, *59*(13), 1541–1552.

Balan, N., and G. J. Bailey (1995a), *Modeling Studies of Equatorial Plasma Fountain and Equatorial Anomaly, Advances in Space Research*, pp. 107–116, vol. 18L, Pergamon Press Ltd, Oxford.

Balan, N., and G. J. Bailey (1995b), Equatorial plasma fountain and its effects—Possibility of an additional layer, *J. Geophys. Res.*, *100*(A11), 21,421–21,432.

Boas, M. (2006), *Mathematical Methods in the Physical Sciences*, vol. 2, John Wiley and Sons, Hoboken, N.J.

Campbell, W. (2003), *Introduction to Geomagnetic Fields*, Cambridge Univ. Press, New York.

Cowling, T. (1932), Magnetism, solar: The electrical conductivity of an ionised gas in the presence of a magnetic field, *MNRAS*, *93*, 90.

Dunham, W. (1990), *Journey Through Genius: The Great Theorems of Mathematics*, John Wiley and Sons, Hoboken, N. J.

Finlay, C. C., et al. (2010), International geomagnetic reference field: The eleventh generation, *Geophys. J. Int.*, *183*(3), 1216–1230.

Fleisch, D. (2008), *A Student's Guide to Maxwell's Equations*, Cambridge Univ. Press, New York.

Forbes, J. M. (1981), The equatorial electrojet, *Rev. Geophys.*, *19*(3), 469–504.

Goldberg, R. A. (1965), Equatorial geomagnetic anomaly and its associated current system, *J. Geophys. Res.*, *70*(21), 5417–5424.

Hapgood, M. A. (1992), Space physics coordinate transformations—A user guide, *Planet. Space Sci.*, *40*(5), 711–717.

Heelis, R. A. (2004), Electrodynamics in the low and middle latitude ionosphere: A tutorial, *J. Atmos. Sol. Terr. Phys.*, *66*(10), 825–838.

Huang, C. (1974), Certain behavior of ionospheric *F*2 region at low latitudes, *Radio Sci.*, *9*(5), 519–532.

Juusola, L., O. Amm, K. Kauristie, and A. Viljanen (2007), A model for estimating the relation between the Hall to Pedersen conductance ratio and ground magnetic data derived from CHAMP satellite statistics, in *Annales Geophysicae, 25*, 721–736.

Kelley, M. (2009), *The Earth's Ionosphere: Plasma Physics and Electrodynamics*, vol. 96, Elsevier: Academic Press, Boston, Mass.

Kivelson, M. G., and C. T. Russell (1995), *Introduction to Space Physics*, Cambridge Univ. Press, New York.

Langel, R. A., and W. J. Hinze (1998), *The Magnetic Field of the Earth's Lithosphere: The Satellite Perspective*, Cambridge Univ. Press, New York.

Lühr, H., and S. Maus (2006), Direct observation of the *F* region dynamo currents and the spatial structure of the EEJ by CHAMP, *Geophys. Res. Lett.*, *33*, L24102, doi:10.1029/2006GL028374.

Lühr, H., S. Maus, M. Rother, and D. Cooke (2002), First in situ observation of night-time *F* region currents with the CHAMP satellite, *Geophys. Res. Lett.*, *29*(10), doi:10.1029/2001GL013845.

Lühr, H., A. Aylward, C. Stolle, T. Spain, M. Förster, P. Ritter, and A. Aruhlia, (2008), Ionospheric current quantification and modelling

for improved magnetic and electric field analyses for Swarm, *Final Report SWIO-SST-FR(2); ESTEC Contract No. 20943/07/NL/JA*, ESA ESTEC (European Space Research and Technology Centre), Noordwijk, Netherlands.

Maus, S., and H. Lühr (2006), A gravity-driven electric current in the Earth's ionosphere identified in CHAMP satellite magnetic measurements, *Geophys. Res. Lett.*, *33*, L02812, doi:10.1029/2005GL024436.

Millward, G., R. Moffett, S. Quegan, and T. Fuller-Rowell (1996), A coupled thermosphere-ionosphere-plasmasphere model (CTIP), in *Solar-Terrestrial Energy Program: Handbook of Ionospheric Models*, edited by R. Schunk, pp. 239–279, Center for Atmospheric and Space Sciences, Utah State University, Logan, Ut.

Mitra, S. K. (1946), Geomagnetic control of region-*F*2 of the ionosphere, *Nature*, *158*(4019), 668–669.

Neubert, T., M. Mandea, G. Hulot, R. von Frese, F. Primdahl, J. L. Jørgensen, E. Friis-Christensen, P. Stauning, N. Olsen, and T. Risbo (2001), Ørsted satellite captures high-precision geomagnetic field data, *Eos Trans. AGU*, *82*(7), 81–88.

Olsen, N. (1997), Ionospheric *F* region currents at middle and low latitudes estimated from Magsat data, *J. Geophys. Res.*, *102*(A3), 4563–4576.

Olsen, N., T. Sabaka, L. Gaya-Pique, A. Kuvshinov, and L. Tøffner-Clausen, (2007), Study of an improved comprehensive magnetic field inversion analysis for Swarm: Final report, *Tech. Rep. DNSC Scientific Report 1/2007*, Danish National Space Center, Copenhagen.

Olsen, N., M. Mandea, T. J. Sabaka, and L. Tøffner-Clausen (2009), CHAOS-2—A geomagnetic field model derived from one decade of continuous satellite data, *Geophys. J. Int.*, *179*(3), 1477–1487.

Reigber, C., H. Lühr, and P. Schwintzer (2002), *CHAMP Mission Status, Advances in Space Research*, pp. 129–134, vol. 30, Pergamon-Elsevier Science Ltd, Oxford.

Richmond, A. D. (1995), Ionospheric electrodynamics using magnetic apex coordinates, *J. Geomagn. Geoelec.*, *47*(2), 191–212.

Rishbeth, H. (1971), F-layer dynamo, *Planet. Space Sci.*, *19*(2), 263–267.

Rishbeth, H. (1988), Basic physics of the ionosphere—A tutorial review, *J. Inst. Electron. Radio Eng.*, *58*(6), S207—S223.

Ritter, P., and H. Lühr (2006), Curl-B technique applied to Swarm constellation for determining field-aligned currents, *Earth Planets Space*, *58*(4), 463–476.

Sabaka, T. J., N. Olsen, and M. E. Purucker (2004), Extending comprehensive models of the Earth's magnetic field with Ørsted and CHAMP data, *Geophys. J. Int.*, *159*(2), 521–547.

Schunk, R. W., and A. Nagy (2009), *Ionospheres: Physics, Plasma Physics, and Chemistry*, Cambridge Univ. Press, Cambridge, U. K.

Stauning, P., and F. Primdahl (2000), First detection of global dawn-dusk ionospheric current intensities using Ampere's integral law on Ørsted orbits, *Geophys. Res. Lett.*, *27*(20), 3273–3276.

Suzuki, A., N. Fukushima, and Sunward or anti-sunward electric current in space below the MAGSAT level (1982), *Geophys. Res. Lett.*, *9*(4), 345–347.

Weisstein, E. (2003), *CRC Concise Encyclopedia of Mathematics,* 2nd ed., CRC Press, Boca Raton, Fla.